

Corrosion behavior of AlSi10Mg alloy produced by laser powder bed fusion under chloride exposure

M. Cabrini^{a,*}, S. Lorenzi^a, T. Pastore^a, C. Testa^a, D. Manfredi^b, M. Lorusso^b, F. Calignano^c, M. Pavese^d, F. Andreatta^e

^aUniversity of Bergamo, Department of Engineering and Applied Science, Viale Marconi, 5 24044 Dalmine, Italy, marina.cabrini@unibg.it; sergio-lorenzi@unibg.it, Tommaso.pastore@unibg.it, Cristian.testa@unibg.it

^bCenter for Sustainable Future Technologies CSFT@PoliTo, Istituto Italiano di Tecnologia, Via Livorno 60, 10144 Torino, Italy, diego.manfredi@iit.it, Massimo.Lorusso@iit.it

^cDipartimento di Ingegneria Gestionale e della Produzione (DIGEP), Politecnico di Torino, Corso Duca degli Abruzzi 24, 10129 Torino, Italy, flaviana.calignano@polito.it

^dDipartimento Scienza Applicata e Tecnologia, Politecnico di Torino, Corso Duca degli Abruzzi 24, 10129 Torino, Italy, matteo.pavese@polito.it

^ePolytechnic Department of Engineering and Architecture, University of Udine, Via del Cottonificio 108, 33100 Udine, Italy, francesco.andreatta@uniud.it

*corresponding author

ABSTRACT

Potentiodynamic tests were performed on AlSi10Mg alloy produced using laser powder bed fusion. As corrosion depends on the surface conditions, we compared the rough as-built surface with that formed after mechanical polishing and passivation in air. The as-built samples showed lower pitting potentials than polished samples. Corrosion initiation depended heavily on the chloride concentration. The higher potential of Si particles compared to the Al matrix provided the driving force for selective dissolution of the α -Al phase. The potential difference between the Si particles and α -Al phase was higher at the melt pool edges, resulting in preferential attack of these regions.

KEYWORDS: A. Aluminium; B. Polarization; C. Pitting corrosion; Anodic dissolution

1. INTRODUCTION

The laser powder bed fusion (LPBF) process, also called selective laser melting (SLM) or direct metal laser sintering (DMLS), is an additive manufacturing (AM) technique that melts metal powders, layer by layer, using a laser controlled by a three-dimensional CAD model [1]. The part is built up by scanning the laser across the powder layer in a set pattern of parallel lines. When the desired shape has been melted, a subsequent layer of powder is added. Compared to traditional subtractive processes, LPBF can reduce costs and manufacturing time, avoid wasted material, and can produce complex parts with undercuts that are not otherwise obtainable [2-3]. The manufacture of aluminum components using this technique requires an optimized laser scanning strategy to avoid the formation of oxides at the interface between adjacent scans and limit porosity development; Al is a challenging material to process due to its high reflectivity and its tendency to oxidize, even in the presence of very small quantities of oxygen [3]. Using Al-based alloys can alleviate some of these problems. Currently, the AlSi10Mg hypoeutectic alloy is considered one of the most suitable alloys for this technique, allowing the production of high-density components with suitable properties [4-6].

The high cooling rate of the trace melted by the laser produces a much finer microstructure than traditional die-casting, resulting in improved mechanical properties [2]. However, components produced

by LPBF have rough surfaces [7], which can degrade the corrosion resistance, which is highly dependent on the surface conditions. The LPBF process, and in general AM processes, are relatively recent; most published studies regarding alloys produced using such techniques are devoted to setting up the best printing conditions, for example to reduce the porosity or improve the mechanical properties [1, 4, 6].

Only a few studies have evaluated the corrosion properties of this alloy, or aluminum alloys in general. Leon et al. [8] and Fathi et al. [9] reported a slight increase in the corrosion resistance of LPBF-produced AlSi10Mg compared to equivalent cast materials, while Gharbi et al. reported similar results for the AA2024 alloy obtained using DMLS [10]. Yang et al. reported that an LPBF-produced Al-12Si alloy had better corrosion resistance than the as-cast Al-12Si alloy in 3.5% NaCl solution [11]. In our previous study, we showed that polishing and shot peening can increase the corrosion resistance of AlSi10Mg [12]. Pickling treatments can improve the corrosion behavior of the as-built surface, but not that of a polished sample; on the contrary, treatment with cerium salt as a corrosion inhibitor is effective only for polished specimens [13].

The lack of systematic data on the corrosion behavior of LPBF-produced alloys is also due to there being several parameters involved in the corrosion mechanism in addition to the surface condition. For example, the building direction, temperature of the building platform, and post-processing heat treatment process must also be taken into account. In particular, the post-processing heat treatment changes the distribution of silicon inside and at the edge of the melt pools. The corrosion morphology changes as consequence of the post-processing heat treatment, from shallow attacks in the untreated samples, to very deep penetration at the edge of the melt pool in samples heat treated at 300°C, and finally to widespread corrosion due to the spherical silicon particles formed at temperatures over 400°C [14]. However, a heat treatment at 300°C is generally employed to relax thermal residual stresses introduced by the laser during processing.

As a systematic study of the corrosion behavior of the AlSi10Mg alloy in a neutral solution has not yet been published, the aim of this study was to evaluate the corrosion resistance of an LPBF AlSi10Mg alloy using potentiodynamic tests in chloride solutions with various concentrations. The corrosion behavior was evaluated by measuring the pitting potential (E_{pit}) as a function of chloride ion activity. As the surface properties are known to affect the corrosion behavior, two surface conditions were studied: the as-built surface as a control, and the other after polishing the as-built surface with abrasive papers and colloidal alumina in order to remove the oxide layer developed during processing.

2. EXPERIMENTAL SECTION

2.1. Materials and specimens

The specimens were prepared using gas-atomized AlSi10Mg alloy powder supplied by EOS GmbH (Electro-Optical Systems, Germany), with the nominal chemical composition shown in Table 1 and a particle diameter range of 0.5–40 μm . During LPBF processing using an EOS M270 Dual Mode machine, equipped with a 200W Yb fiber laser, good connection between two successive layers was ensured by adjusting the laser beam intensity to achieve complete melting of the new powder layer and laser penetration into the previous layer. On the basis of previous studies in which the main process parameters were optimized to obtain fully dense components [2], the samples were built using a power of 195 W, scanning speed of 800 mm/s, hatching distance of 0.17 mm, layer thickness of 0.03 mm, and temperature of the building platform of 100°C. Moreover, the scanning direction was rotated 67° between consecutive layers in order to achieve optimal overlapping [2]. Disk specimens with a diameter of 15 mm and height of 5 mm were fabricated and analyzed. The specimens were built with the circular surface perpendicular to the building platform (*xy plane*), or parallel to the so-called building direction (*z axis*).

These specimens are henceforth referred to as as-built (AB) samples, which showed a high surface

roughness (Fig. 1 (a)). Some AB specimens were ground with abrasive paper down to 4000 grit, polished with 0.3 μm colloidal alumina, then left for 48 h in ambient conditions in the laboratory to form a spontaneous passive film before further testing; these samples are henceforth referred to as polished (P) samples (Fig. 1 (b)). The roughness values of the AB specimens were reported in a previous study [7]; the average surface roughness (R_a) was 23 μm with a maximum distance between the highest peak and lowest valley (R_z) of 153 μm . A residual porosity of 0.7–0.8% was measured. Before electrochemical testing, all specimens were degreased using acetone.

2.2. Potentiodynamic tests

Potentiodynamic polarization tests were performed using an Ivium CompactStat with a 1-L ASTM G5-82 glass cell, equipped with a saturated calomel reference electrode (SCE) placed in a Huber-Luggin capillary probe, and two graphite counter electrodes. The specimens were inserted into a PTFE sample holder with an exposed surface of 0.785 cm^2 and used as the working electrode. The specimens were immersed in the solution and stabilized for 600 s at the free corrosion potential (E_{cor}). The tests were carried out at 23°C in aerated NaCl solutions, with a concentration ranging from 0.01 to 0.6 mol/L. Na_2SO_4 was added to the solutions as a supporting electrolyte in order to maintain a constant Na^+ ion concentration (~ 0.6 M) and avoid significant differences in electrical conductivity. Table 2 summarizes the composition of the test solutions and lists the activity coefficient (γ_{Cl^-}) estimated according to Dash et al. [15], and the corresponding activity of chloride ions (a_{Cl^-}) calculated as the product between the molar concentration and the activity coefficient.

Before each test, the Ohmic drop in the solution was evaluated by measuring the electrode impedance between 1000 and 40000 Hz, with an amplitude of 20 mV vs. E_{cor} . The obtained Ohmic resistance, normally between 4–5 Ωcm^2 , was then subtracted from the potential measured for the samples. This contribution became appreciable (> 1 mV) for current densities above 200 $\mu\text{A}/\text{cm}^2$. The potentiodynamic tests were conducted with a potential scan rate of 0.1667 mV/s, from -20 mV vs E_{cor} up to an anodic current density of 10 mA/cm^2 . The value above which a rapid increase in the current occurred was assumed to be the pitting potential. Two or more tests for each condition were carried out.

2.3. Scanning Kelvin probe force microscopy

The scanning Kelvin probe force microscopy (SKPFM) technique was used to obtain topographic and surface potential (Volta potential) maps of polished AlSi10Mg specimens with a Nanoscope III multimode atomic force microscope (AFM) equipped with an Extender TM electronic module. The maps were acquired using n^+ -silicon tips coated with PtIr₅ at 23°C with a relative humidity of 40–65%. The topography and potential maps were sampled with a scan frequency of 0.1 Hz. To acquire potential maps, we used a scan height of 100 nm in the lift mode.

3. RESULTS AND DISCUSSION

Fig. 2 shows the corrosion potentials (E_{cor}) of the specimens after 500 s of immersion; the average value measured over the subsequent 100 s was considered. The standard deviation of the 100 points acquired was < 5 mV for all specimens, indicating that the values were stable after the 500 s immersion. The E_{cor} values of the P specimens were slightly more noble than those of the AB specimens. There was a steady decrease in E_{cor} with increasing chloride concentration in the solution due to an increase in the current density in the passive range of the curve.

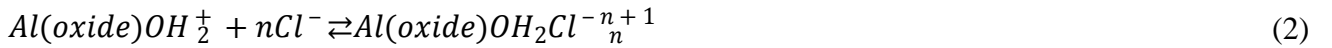
Fig. 3 (a) shows the potentiodynamic curves of a P specimen as a function of the activity of the chloride ions in solution. At low chloride concentrations, a clear range of passivity was observed, where the onset potential for localized corrosion decreased with increasing chloride concentration in the

solution, until the typical trend of a Tafel line was observed; this indicated an active behavior of the metal in the solution with 3.5% of NaCl ($a_{Cl^-} = 0.05$ mole/L). The latter behavior of the potentiodynamic polarization curve indicated that localized corrosion was triggered during the initial conditioning period of the specimen in solution at the corrosion potential. In this case, the corrosion potential was assumed to be the pitting potential [16]. The potentiodynamic polarization curves of the AB specimens (Fig. 3 (b)) showed a passive range only in the solutions with the lower chloride concentrations, while in all other solutions the current density suddenly increased, indicating that localized attacks were initiated during the equilibration time. The passive range was shorter than that of the P specimens. The appearance of localized corrosion on the exposed surface of all specimens was evident independent of the surface condition (as shown by the SEM images shown in Fig. 4 (a) and (b)) and the chloride concentration (Fig. 4 (c) and (d)). Selective dissolution of the edge of the melt pools was consistently observed.

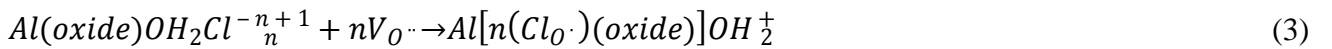
The corrosion mechanism of aluminum in chloride solutions has been described in numerous studies [17-21]. According to the McCafferty model [19, 23], the surface of the aluminum passive film assumes a positive charge when it is immersed in a solution with a pH lower than the zero point of charge of its oxide (~8.9–9.2), according to Eq. (1).



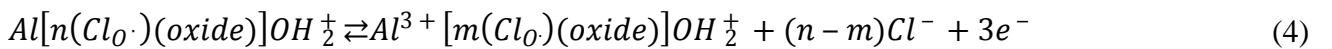
In this reaction, $Al(oxide)$ indicates the metallic Al and the adjacent oxide layer, while OH represents the outer layer of oxide surface hydroxyl groups. The positive charge of the passive film attracts chloride ions from solution, as shown in Eq. (2), where n is the number of chloride ions interacting with the surface.



These ions diffuse for a second time inside the oxide via oxygen vacancies ($V_{O^{\cdot}}$), according to the reaction:



In Eq. (3), $Cl_{O^{\cdot}}$ represents the ions occupying the oxygen sites in the oxide lattice and $Al[n(Cl_{O^{\cdot}})(oxide)]OH^{\frac{+}{2}}$ is the oxide film on the aluminum side where the diffusion of chloride ions takes place; the aluminum at the metal–oxide interface is involved in a three-stage process, losing three electrons, as described by the overall reaction:



Frankel [18] demonstrated that the stable propagation of the pit occurs when critical environmental conditions occur that no longer allow repassivation of the metal. Chloride ions prevent repassivation; a critical concentration of Cl^- in the film is therefore necessary to allow propagation of the pit. The total current density (i_a) of the anodic process can be written as a sum of two terms, as shown in Eq. (5), where i_u is the current density of the process that takes place uniformly over the passive surface and i_{pit} is the contribution from the formation of localized pits [19].

$$i_a = i_u + i_{pit} \quad (5)$$

In addition to transient phenomena related to the potential scanning rate, i_u corresponds to the passivity current. The term i_{pit} is zero under passive conditions, while it assumes a non-zero value when the

potential (E) exceeds the pitting potential (E_{pit}) and the attack is initiated. During the propagation phase of pitting corrosion, i_{pit} is significantly larger than i_u . Considering the equilibrium conditions for the reaction shown in Eq. (4), McCafferty [19] proposed a relationship between E_{pit} and a_{Cl^-} , valid at constant pH:

$$\left(\frac{dE_{pit}}{d \log[Cl^-]} \right)_{pH} = \frac{-n}{\frac{5}{2} \cdot \left(\frac{E}{2.303RT} \right)} = \text{constant} \quad (6)$$

This relationship was verified by observation of a linear trend when plotting the relevant experimental variables on a semi logarithmic scale in several previous studies [22-24]. According to Eq. (6), the gradient of E_{pit} vs. a_{Cl^-} is proportional to the number of chloride ions, n , diffusing into the oxide via oxygen vacancies, following Eq. (2) and (3). According to this model, the different gradients are due to the different concentrations of chloride ions required to initiate pitting, where higher slopes correspond to a greater resistance to the initiation of pitting.

The experimental pitting potential values (Fig. 5) decreases with the increasing of the chloride ion activity. The linear relationship proposed by McCafferty [19] seems not to strictly fit data due to relevant scattering. Such model was developed for pure aluminum, whilst AlSi10Mg alloy contains silicon particles more noble than the Al matrix. The galvanic effect of these precipitates could promote pitting and the variations in the local pH caused by the cathodic reaction can affect the passive film stability of aluminum.

The pitting potential can be determined only in the case in which the localized corrosion is initiated during the potentiodynamic test. This condition was observed only for the P specimens at the lower chloride concentrations. The data for the P specimens had a gradient of about -0.540 V/decade. When the pitting is initiated during the equilibration time at the beginning of the test, the pitting potential overlaps the corrosion potential. This condition was observed for one P specimen (of a total of three) at $a_{Cl^-} = 0.05M$ and for all the P specimens tested in solutions of $a_{Cl^-} = 0.34 M$. The values of these specimens overlapped the linear trend of the AB specimens, which always showed initiation of pitting during the equilibration time, before starting the potentiodynamic scan. The curve of this data had a gradient of about -0.058 V/decade, which is one order of magnitude lower than that of the P specimens, indicating a much smaller resistance to initiation of pitting. An increase in the corrosion resistance of Al-10Si-Mg specimens after polishing has previously been reported [12, 25].

The higher resistance to the initiation of localized corrosion of the P specimens compared with the AB ones was confirmed by analysis of the of the polarization resistance (R_p) values measured in the range of ± 10 mV vs. E_{cor} . The value i_a (Eq. (5)) was calculated, as shown by Evans and Koehler [26] using the Stern–Geary relationship and the polarization resistance:

$$i_a = \frac{k}{R_p} \quad (7)$$

Here, k can be evaluated using the slopes of the polarization curves of the anodic (b_a) and cathodic (b_c) process using the following relationship:

$$k = \frac{b_a b_c}{2.3(b_a + b_c)} \quad (8)$$

If the alloy is passive, the slope of the anodic polarization curve is much higher than that of the cathodic one, which was ~ 120 mV/decade and coincided with that of the hydrogen cathodic process, as the oxidation process is current limited at low potential. This resulted in a k value of 52 mV. In this case, i_{pit}

did not contribute to the total anodic current, and i_a coincided with i_u . Fig. 6 shows the corresponding i_u values as a function of a_{Cl^-} for the P specimens that remained passive during the equilibration time. On the contrary, for the AB specimens, for which the pitting was initiated during the equilibration time, the value of the current density measured by means of the R_p gave the value for i_a . In this case, we determined a k value of 26 mV/decade, consistent with an active corrosion process. A linear correlation between i_a and a_{Cl^-} was also observed, with values one order of magnitude higher than those of the P samples. This difference can be ascribed to the difference in the exposed areas (due to the higher roughness of the AB specimens compared to the P specimens), and to the contribution of the active dissolution of the alloy inside the pit.

3.1. Effect of surface condition on pitting initiation

The different behaviors of the P and AB specimens can be explained considering the different passive film properties, where the former was spontaneously formed in air, and the latter formed during processing and subsequent heat treatment. During the LPBF process, the oxide film was initially formed during solidification in the argon chamber, in an environment with a very low oxygen partial pressure. Subsequently the oxide film grew during the heat treatment used to reduce the residual internal strains introduced during processing. Polishing removed the oxide film present on the AB specimens, which allowed reformation of a film more resistant to the action of the chlorides. Furthermore, as the surface roughness was reduced, the number of critical sites for pitting initiation also decreased. However, polishing cannot completely eliminate residual pores on the surface, which act as preferential sites for pit initiation. The onset of pitting at these sites can explain the experimental data that deviates from the usual behavior of the polished surface, approximating those obtained on the unpolished as-built surface, as the internal porosity of the P specimens with the passive film was the same as that of the AB specimens.

The composition of the oxides formed on AB and P specimens was investigated using XPS, as reported in our previous study [13]. The AB specimens showed a superficial oxygen concentration higher than that of the P specimens (Fig. 7). The hot-formed oxide was rich in oxygen, while the aluminum profile indicated an Al-poor surface. Therefore, the surface oxides on the AB and P samples had different compositions, but they maintained the same acid–base properties, as noted by Van den Brand et al. [27], as oxides formed spontaneously in air or oxidized at high temperature. According to Pech-Canul et al. [28], the oxide formed on the Al-12% alloy incorporates silicon and silicon oxide particles, which makes it more resistant to pitting initiation than pure Al. These particles inhibit chloride from penetrating and diffusing through the film. However, in this case, although the alloy had a Si concentration of ~10%, significant concentrations of Si were not observed either in the passive film present on the AB specimens, nor in the oxide spontaneously formed on the P specimens (Fig. 7).

Vargel [29] described the spontaneous oxide formed in air on Al surfaces as consisting of two layers. The inner layer of about 4 nm thick, present at the metal–oxide interface, acts as a barrier against corrosion, is compact, amorphous, and forms immediately upon contact of the metal surface with air, regardless of the temperature. Its kinetics of formation does not depend on the oxygen partial pressure, while the thickness of the second layer of the film depends on temperature. The latter grows on the barrier layer as a result of the hydration reaction with atmospheric moisture. The final thickness is reached only after several weeks, sometimes even months, and depends on the environment. High-temperature treatment modifies the morphology of the passive film, increasing its thickness and crystallinity, while increasing the porosity and producing microcracks, which decrease the corrosion resistance compared to amorphous films. Such mechanisms may explain the lower E_{pit} values observed for the AB specimens compared to the P specimens.

3.2. Pitting propagation and selective attack

After pit initiation, a series of processes takes place that forms occluded cells. Al ions dissolved from the metal hydrolyze and produce an acidic environment, while the chloride ions migrate and concentrate inside the cell. The very low aluminum nobility allows the evolution of hydrogen at any pH and allows the cathodic process to sustain itself inside the pit without an external oxygen supply or presence of a conductive passive film on adjacent regions.

Considering the LPBF specimens produced here, regardless of the surface conditions, the pit growth proceeded by selective dissolution of the α -Al phase, due to its atypical microstructure. This alloy has an inhomogeneous microstructure very different from that observed for alloys of a similar composition obtained by casting or for wrought alloys. On the surface of the AB sample, two distinct areas were observed in the microstructure, as shown in Fig. 8: (i) melt pools formed by the laser trace and (ii) edges of the melt pools, between adjacent tracks. Inside the melt pools, we observed Si-rich microdendrites of Al with silicon particles and the α -Al/Si eutectic [3]. The edge of the melt pool experienced double fusion and showed an adjacent heat-affected zone (HAZ). The HAZ was subjected to a second heating during laser scanning of adjacent areas, but experienced a temperature lower than the melting temperature, and showed partial recrystallization [2]. The main effects of these microstructural variations were a change in the solidification direction of the dendrites and the formation of a zone in which the α -Al phase was present, with isolated idiomorphic Si crystals. The successive heat treatment at 300°C removed the eutectic α -Al/Si phase, and the Si particles coalesced to form a continuous network decorated with α -Al dendrites (Fig.8 (c) and (d))[3]. In the HAZ, the isolated idiomorphic crystals of Si grew inside the α -Al matrix (Fig. 8 (d)). This particular microstructure resulted in selective attack after pitting initiation, with preferential corrosion of the edge of the melt pool (Fig. 4). The attack progressed via selective dissolution of the α -Al matrix, stimulated by the higher nobility of the Si particles, which acted as cathodes [30].

Fig. 9 shows an SEM micrograph of a region of a P specimen, along with its corresponding potential map and EDS maps. The continuous network of Si-rich particles visible in the SEM image (Fig. 9 (a)) produces the regions of bright contrast in the potential map (Fig. 9 (b)). The EDS maps for Al and Si (Fig. 9 (c) and (d), respectively) confirmed that regions with higher potential were Si-rich particles, indicating that these particles have cathodic behavior relative to the adjacent α -Al dendrites. Fig. 10 shows a high-resolution potential map of the edge of a melt pool (indicated by the dashed line in Fig.10 (a)). A potential profile along the black line shown in Fig. 10 (a) is shown in Fig. 10 (b), which indicated that the difference in potential between the Si-rich particles and the α -Al phase tended to be higher near the edge of the melt pool (~100 mV) than in the center of the α -Al dendrite (e.g., 50 mV at a distance of ~5 μ m from the melt pool edge). Similar results were reported by Revilla et al. [31] for as-built specimens without heat treatment, where they measured higher absolute potential values (222 mV between Si and Al at the edge and 95 mV at the center). In the regions of localized attack along the edges of the melt pools, it is likely that local acidification prevented reformation of the passive film, leading to preferential corrosion of the Al matrix. The attack also occurred within the melt pools, which was partially shielded by the network of Si decorating the Al microdendrites [12], reducing the penetration of the attack. In this way, the melt pool edge was a preferential path for corrosion (Fig. 4).

As reported previously [14], heat treatment at 300°C promoted localized attack at the edges of the melt pools and was avoided using higher building platform temperature; for aerospace applications a temperature of 200°C is recommended. If stress relief is necessary, use of a heat-treatment temperature higher than 400°C could destroy the melt pool macrostructure and avoid selective dissolution of the melt pool edges. Unfortunately, such high temperatures greatly decrease the hardness and increase overall

corrosion [25]. On-going studies are evaluating the effect of the heat treatment on the pitting potential of the alloy.

CONCLUSIONS

The paper studied the effect of chloride ions concentration on the pitting initiation of an AlSi10Mg alloy obtained by means of laser powder bed fusion with as built and polished surface. The main results obtained can be summarized as follows:

- A significant different corrosion behavior between the rough and polished surfaces was observed at chloride ion activities lower than 0.05 M, while it was negligible for high chloride concentrations.
- The experimental data showed a logarithmic correlation between the pitting potential and activity of chloride ions in solution for the polished specimens.
- After film breakdown and localized corrosion initiation, the attack proceeded by selective dissolution of the α -Al phase along the edges of melt pools, due to the presence of more noble precipitates of silicon; therefore, in the same way for as built and polished ones.
- As observed using scanning Kelvin probe force microscopy (SKPFM) technique, the potential difference between Si-rich particles and the α -phase tended to be higher at the melt pool edges, favoring the preferential attack of these regions.

Funding

This research did not receive any specific grant from funding agencies in the public, commercial, or not-for-profit sectors.

Data Availability

The raw/processed data required to reproduce these findings cannot be shared at this time as the data also forms part of an ongoing study.

REFERENCES

- [1] W.E Frazier, Metal additive manufacturing: A review, *J. Mat. Eng. Perf.* 23 (2014) 1917–1928.
- [2] F. Trevisan, F. Calignano, M. Lorusso, J. Pakkanen, A. Aversa, E.P. Ambrosio, M. Lombardi, P. Fino, D. Manfredi, On the selective laser melting (SLM) of the AlSi10Mg alloy: Process, microstructure, and mechanical properties, *Materials* 10 (2017) 76-99: DOI: 10.3390/ma10010076.
- [3] K. Louvis, L. Fox, C.J. Sutcliffe, Selective laser melting of aluminum components. *J. Mat. Proc. Tech.* 211 (2011) 275–284.
- [4] E.O. Olakanmi. Selective laser sintering/melting (SLS/SLM) of pure Al, Al–Mg, and Al–Si powders: Effect of processing conditions and powder properties, *J. Mater. Process. Technol.* 213 (2013) 1387–1415.
- [5] L. Thijs, K. Kempen, J.-P. Kruth, J. Van Humbeeck, Fine-structured aluminum products with controllable texture by selective laser melting of pre-alloyed AlSi10Mg powder, *Acta Mater.* 61 (2013) 1809–1819.
- [6] N.T. Aboulkhair, N.M. Everitt, I. Ashcroft, and C. Tuck, Reducing porosity in AlSi10Mg parts processed by selective laser melting, *Add. Manuf.* 1 (2014) 77–86.
- [7] F. Calignano, D. Manfredi, E. Ambrosio, L. Iuliano, P. Fino. 2013, Influence of process parameters on surface roughness of aluminum parts produced by DMLS, *Int. J. Adv. Manuf. Technol.* 67: 2743–2751.
- [8] A. Leon, A. Shirizly, E. Aghion, Corrosion behavior of AlSi10Mg alloy produced by additive manufacturing (AM) vs. its counterpart gravity cast alloy, *Metals (MPDI)* 6(7) (2016) 148; doi:10.3390/met6070148.
- [9] P. Fathi, M. Mohammadi, X. Duan, A.M. Nasiri, A comparative study on corrosion and microstructure of direct metal laser sintered AlSi10Mg_200C and die cast A360.1 aluminum, *J. Mat. Process. Tech.* 259 (2018) 1–14.
- [10] O. Gharbi, D. Jiang, D.R. Feenstra, S.K. Kairy, Y. Wu, C.R. Hutchinson, N. Birbilis, On the corrosion of additively manufactured aluminum alloy AA2024 prepared by selective laser melting, *Corrosion Sci.* 143 (2018) 93-106.
- [12] M. Cabrini, S. Lorenzi, T. Pastore, S. Pellegrini, D. Manfredi, P. Fino, S. Biamino, C. Badini, Evaluation of corrosion resistance of Al–10Si–Mg alloy obtained by means of direct metal laser sintering, *J. Mat. Process. Tech.* 231 (2016) 326–335.
- [13] M. Cabrini, S. Lorenzi, T. Pastore, S. Pellegrini, M. Pavese, P. Fino, E.P. Ambrosio, F. Calignano, D. Manfredi, Corrosion resistance of direct metal laser sintering AlSiMg alloy, *Surf. Interface Anal.* 48 (2016) 818–826.
- [14] M. Cabrini, F. Calignano, P. Fino, S. Lorenzi, M. Lorusso, D. Manfredi, C. Testa, T. Pastore, Corrosion behavior of heat-treated AlSi10Mg manufactured by laser powder bed fusion, *Materials* 11 (2018) 1051.
- [15] D. Dash, S. Kumar, C. Mallika, U. Kamachi Mudali, New data on activity coefficients of potassium, nitrate, and chloride ions in aqueous solutions of KNO₃ and KCl by ion selective electrodes, *ISRN Chem. Eng.* (2012) 7301545.
- [16] M. Ferri, M. Trueba, S.P. Trasatti, M. Cabrini, A. Lo Conte., Electrochemical investigation of corrosion and repassivation of structural aluminum alloys under permanent load in bending, *Corrosion Rev.* 35 (2017) 225–239.
- [17] Z. Szklarska-Smialowska, Pitting corrosion of aluminum, *Corrosion Sci.* 41 (1999) 1743–1767.
- [18] G.S. Frankel, Pitting corrosion of metals A review of the critical factors, *J. Electrochem. Soc.* 145 (1998) 2186–2198.
- [19] E. McCafferty, The electrode kinetics of pitting initiation on aluminum, *Corrosion Sci.* 37 (1995) 481–492.
- [20] P.M. Natishan, W.E. O’Grady. ion interactions with oxide-covered aluminum leading to pitting

- corrosion: A review, *J. Electrochem. Soc.* 161 (2014) C421–C432 doi: 10.1149/2.1011409jes.
- [21] R.T. Foley, Localized corrosion of aluminum alloys: A review, *Corrosion* 42 (1986) 277–288.
- [22] J.R. Galvele S.M: De Micheli. 1970, Mechanism of intergranular corrosion of Al-Cu alloys, *Corrosion Sci.*, 10 (11): 795–807.
- [23] B.N. Stirrup, N.A. Hampson, I.S. Midgley, Pit formation in relation to the etching of aluminum in chloride solutions, *J. Appl. Electrochem.* 5 (1975) 229–235.
- [24] H. Böhni, H.H. Uhlig, Environmental factors affecting the critical pitting potential of aluminum, *J. Electrochem. Soc.* 111 (1969) 906–910.
- [25] M. Cabrini, S. Lorenzi, T. Pastore, S. Pellegrini, E.P. Ambrosio, F. Calignano, D. Manfredi, M. Pavese, P. Fino, Effect of heat treatment on corrosion resistance of DMLS AlSi10Mg alloy , *Electrochim. Acta* 206 (2016) 346–355.
- [26] S. Evans, E.L. Koehler, Use of polarization methods in the determination of the rate of corrosion of aluminum alloys in anaerobic media , *J. Electrochem. Soc.* 108 (1961) 509–514.
- [27] J. van den Brand, P.C. Snijders, W.G. Sloof, H. Terryn, J.H.W. de Wit, Acid-base characterization of aluminum oxide surfaces with XPS, *J. Phys. Chem. B* 108 (2004) 6017–6024.
- [28] M.A. Pech-Canul, M.I. Pech-Canul, P. Bartolo-Pérez, and M. Echeverría, The role of silicon alloying addition on the pitting corrosion resistance of an Al-12 wt.%Si alloy, *Electrochim. Acta* 140 (2014) 258–265.
- [29] C. Vargel, *Corrosion of aluminum*. Vol. 1. Elsevier Ltd., Oxford UK 2004.
- [30] Z.X. Liang, B. Ye, L. Zhang, Q.G. Wang, W.Y. Yang, Q.D. Wang, A new high-strength and corrosion resistant Al-Si based casting alloy, *Mat. Lett.* 97 (2013) 104–107.
- [31] R.I. Revilla, J. Liang, S. Godet, I. de Graeve, Local corrosion behavior of additive manufactured AlSiMg alloy assessed by SEM and SKPFM, *J. Electrochem. Soc.* 164 (2017) C27–C35.

Table 1. Nominal chemical composition of the alloy powder.

Element	Si	Fe	Cu	Mn	Mg	Ni	Zn	Ti	Al
wt. %	9–11	≤0.55	≤0.05	≤0.45	0.2–0.45	≤0.05	≤0.1	≤0.15	balance

Table 2. Composition of the test solutions and their corresponding activity coefficient (γ_{Cl^-}) and activity of chloride ions (a_{Cl^-}).

NaCl		Na ₂ SO ₄ (g/L)	pH	γ_{Cl^-}	a_{Cl^-} (mole/L)
(g/L)	(mole/L)				
0.5	0.01	41.89	7	0.962	0.008
1	0.02	41.18	7	0.858	0.015
3.5	0.06	38.34	7	0.785	0.05
35	0.6	0	7	0.563	0.34

Figure captions

Fig. 1. Representative SEM images of the surfaces of an (a) AB sample and (b) P sample.

Fig. 2. Corrosion potentials (E_{cor} vs. SCE) as a function of chloride concentration. The mean values were collected over 100 s, after 500 s of immersion.

Fig. 3. Effect of chloride ion activity on the polarization curves of (a) P samples and (b) AB samples measured in aerated NaCl solutions at pH 7.

Fig. 4. SEM images of the corrosion morphology of (a) P and (b) AB specimens after potentiodynamic tests in aerated 1 g/L NaCl at 23°C. (c) P specimen after the potentiodynamic tests in aerated 3.5 g/L NaCl at 23°C. (d) Magnified view of the selective attack at the border of the melt pool shown in (c).

Fig. 5. Effect of chloride ion activity on the pitting (filled symbols) and corrosion potential (open symbols) of P and AB specimens in an aerated NaCl solution at 23°C. The corrosion potentials were measured when pitting started during the equilibration time, before the potentiodynamic tests.

Fig. 6. Effect of chloride ion activity on the current density i_u of P samples and i_a ($i_u + i_{pit}$) for AB specimens, evaluated using the polarization resistance.

Fig. 7. XPS spectra measured during milling of the oxide films on the (a) P and (b) AB specimens.

Fig. 8. Cross-sectional microstructure of the as-built AlSi10Mg alloy parallel to the growth direction. (a) Optical microscopy image of the macrostructure. (b) SEM image of the melt pool interface. (c) Higher magnification images of the center and (d) edge of the melt pool (in the box close up at high magnification of the idiomorphic particles of silicon)

Fig. 9. (a) SEM image, (b) SKPFM potential map, and EDS maps of (c) Al and (d) Si for a polished AlSi10Mg LPBF sample.

Fig. 10. (a) SKPFM potential map of a region near the edge of a melt pool (indicated by the white dashed line) and (b) the corresponding potential profile along the black line indicated in (a).

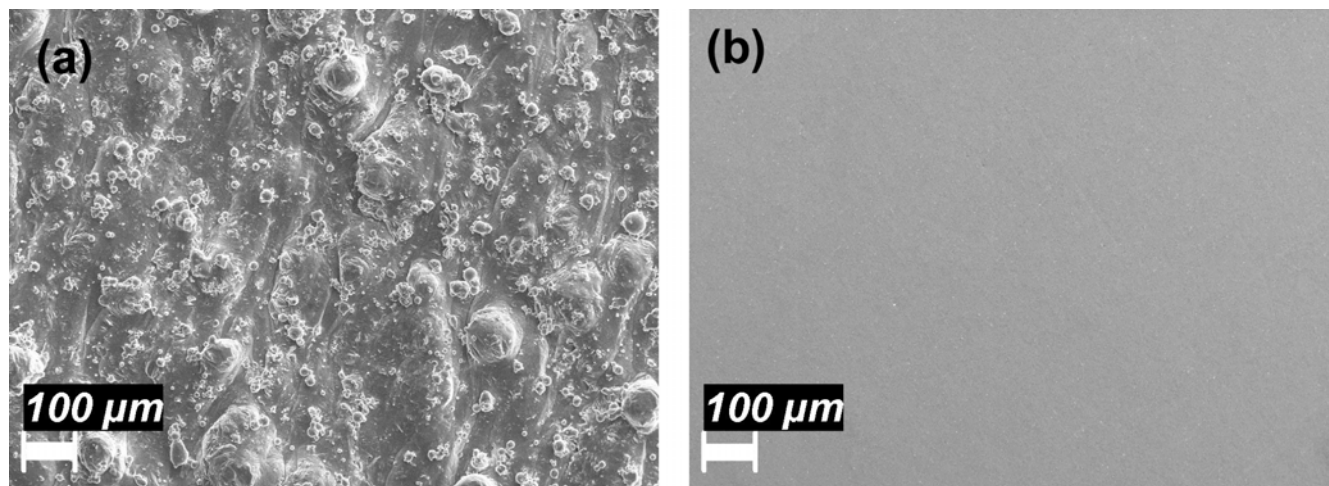


Fig. 1. Representative SEM images of the surfaces of an (a) AB sample and (b) P sample.

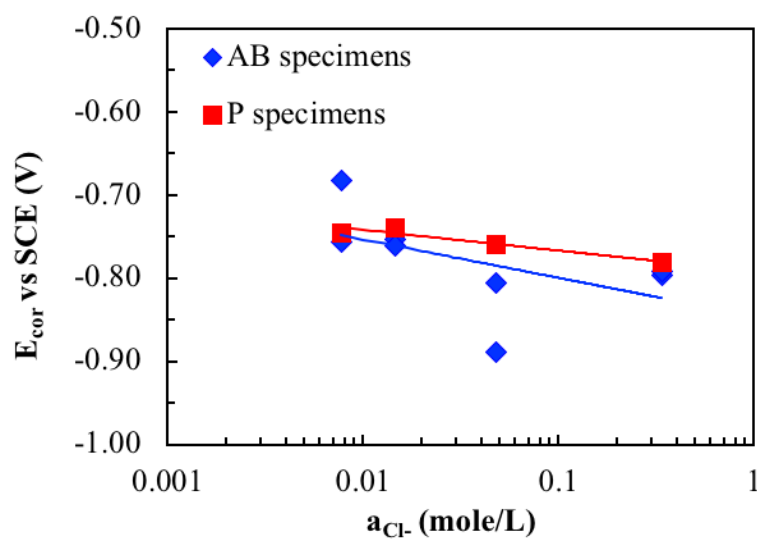
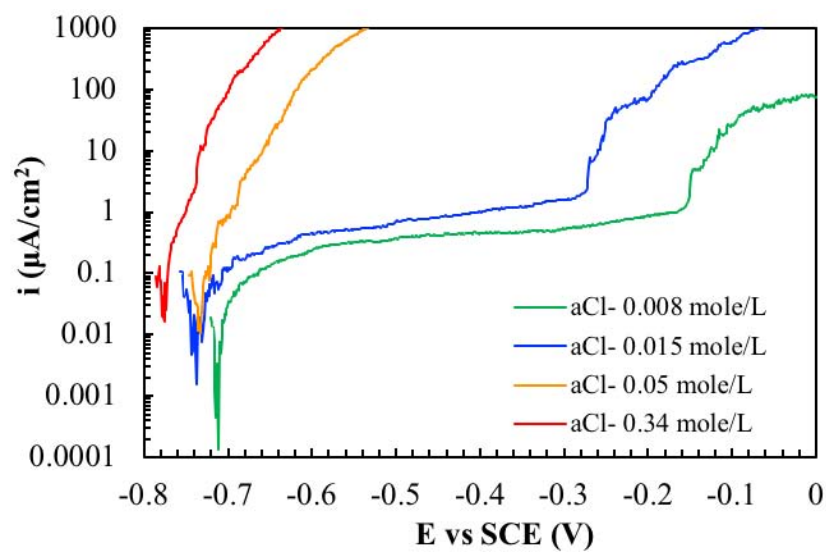
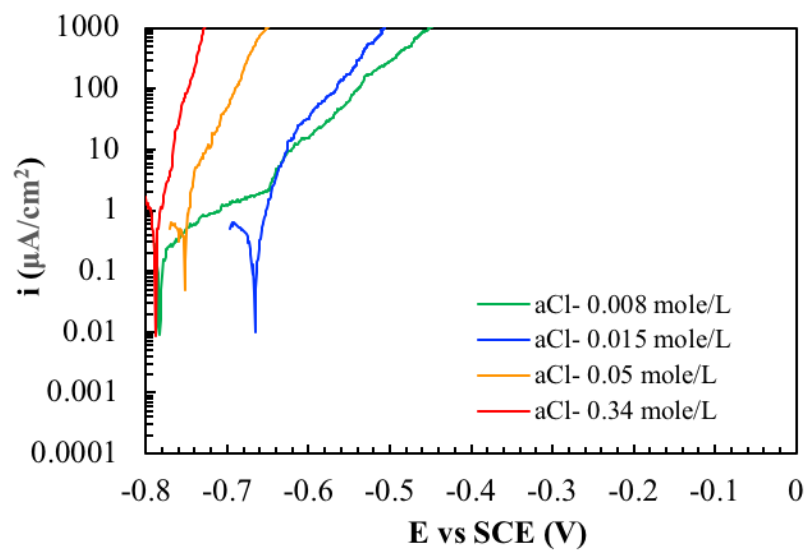


Fig. 2. Corrosion potentials (E_{cor} vs. SCE) as a function of chloride concentration. The mean values were collected over 100 s, after 500 s of immersion.



a)



b)

Fig. 3. Effect of chloride ion activity on the polarization curves of (a) P samples and (b) AB samples measured in aerated NaCl solutions at pH 7.

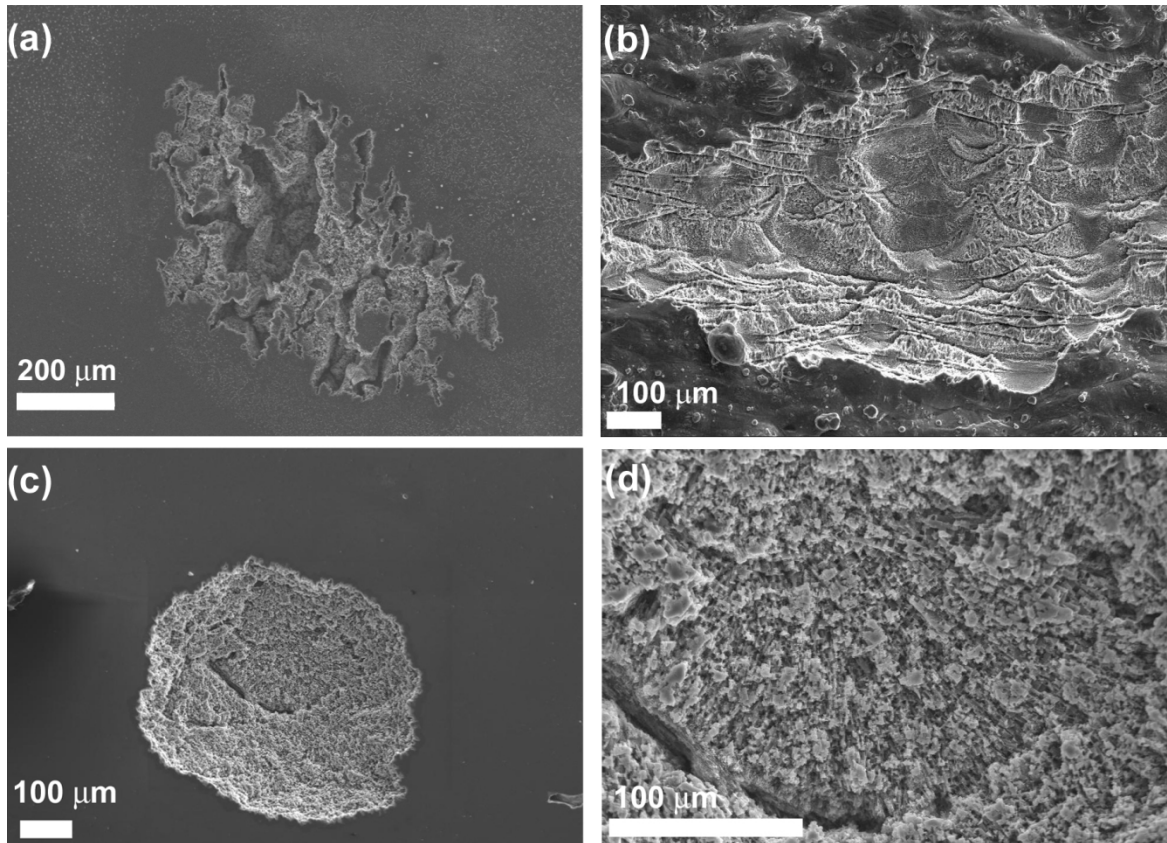


Fig. 4. SEM images of the corrosion morphology of (a) P and (b) AB specimens after potentiodynamic tests in aerated 1 g/L NaCl at 23°C. (c) P specimen after the potentiodynamic tests in aerated 3.5 g/L NaCl at 23°C. (d) Magnified view of the selective attack at the border of the melt pool shown in (c).

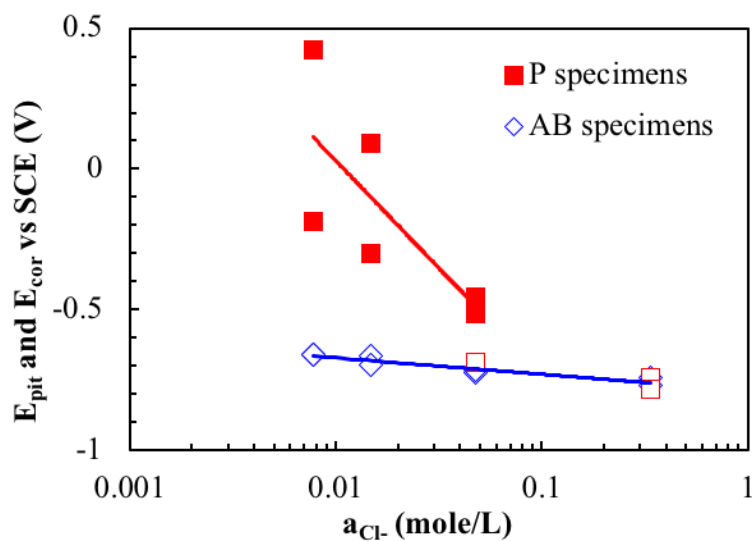


Fig. 5. Effect of chloride ion activity on the pitting (filled symbols) and corrosion potential (open symbols) of P and AB specimens in an aerated NaCl solution at 23°C. The corrosion potentials were measured when pitting started during the equilibration time, before the potentiodynamic tests.

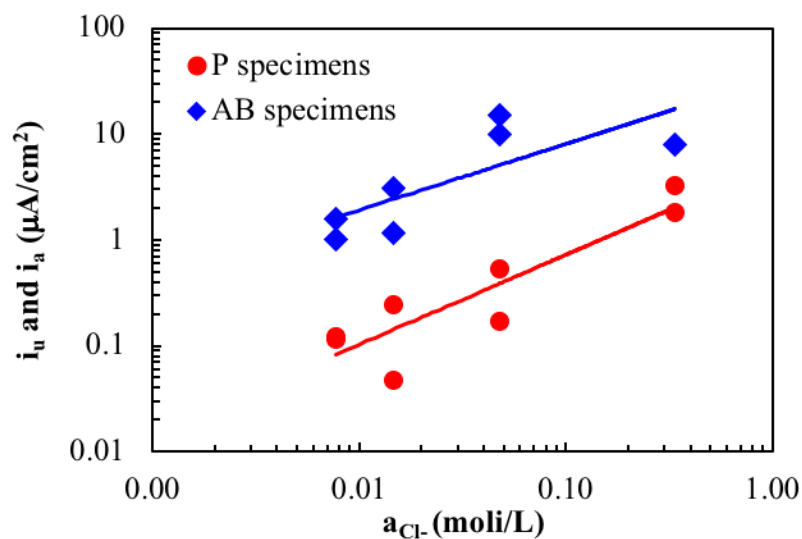
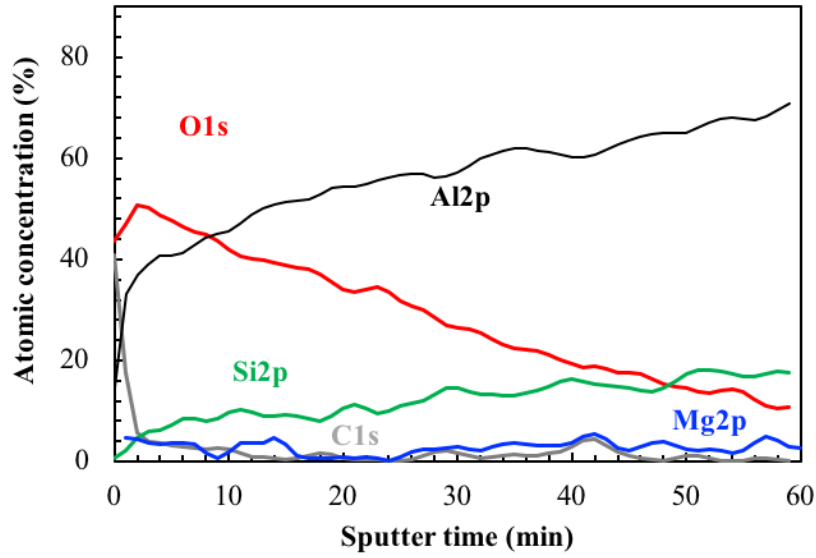
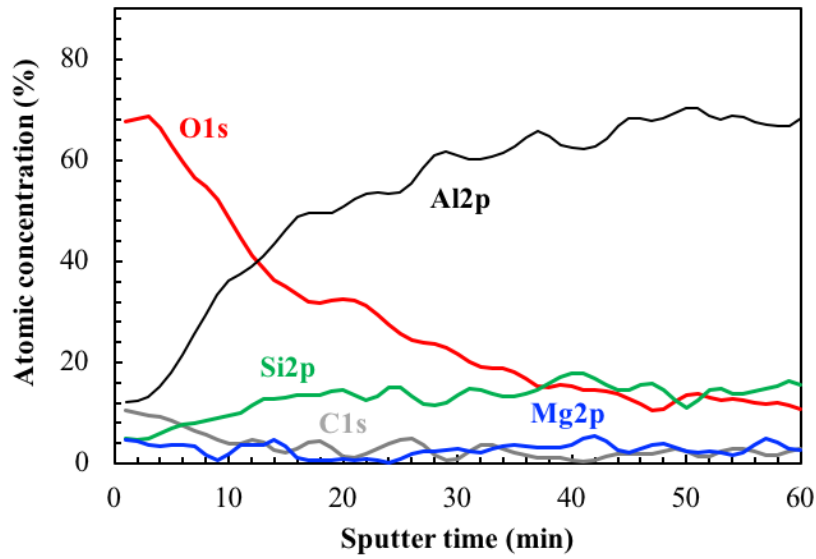


Fig. 6. Effect of chloride ion activity on the current density i_u of P samples and i_a ($i_u + i_{pit}$) for AB specimens, evaluated using the polarization resistance.



a)



b)

Fig. 7. XPS spectra measured during milling of the oxide films on the (a) P and (b) AB specimens.

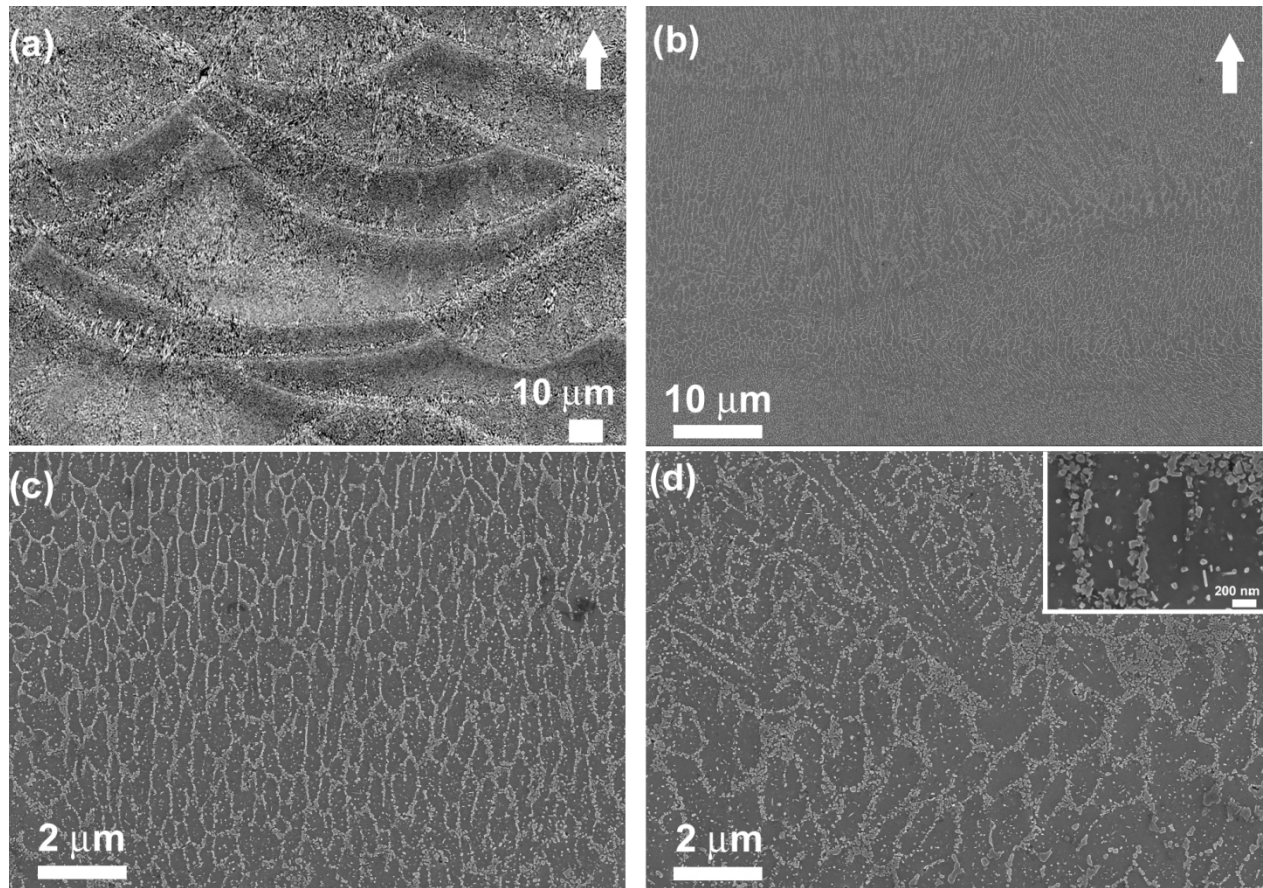


Fig. 8. Cross-sectional microstructure of the as-built AlSi10Mg alloy parallel to the growth direction. (a) Optical microscopy image of the macrostructure. (b) SEM image of the melt pool interface. (c) Higher magnification images of the center and (d) edge of the melt pool (in the box close up at high magnification of the idiomorphic particles of silicon)

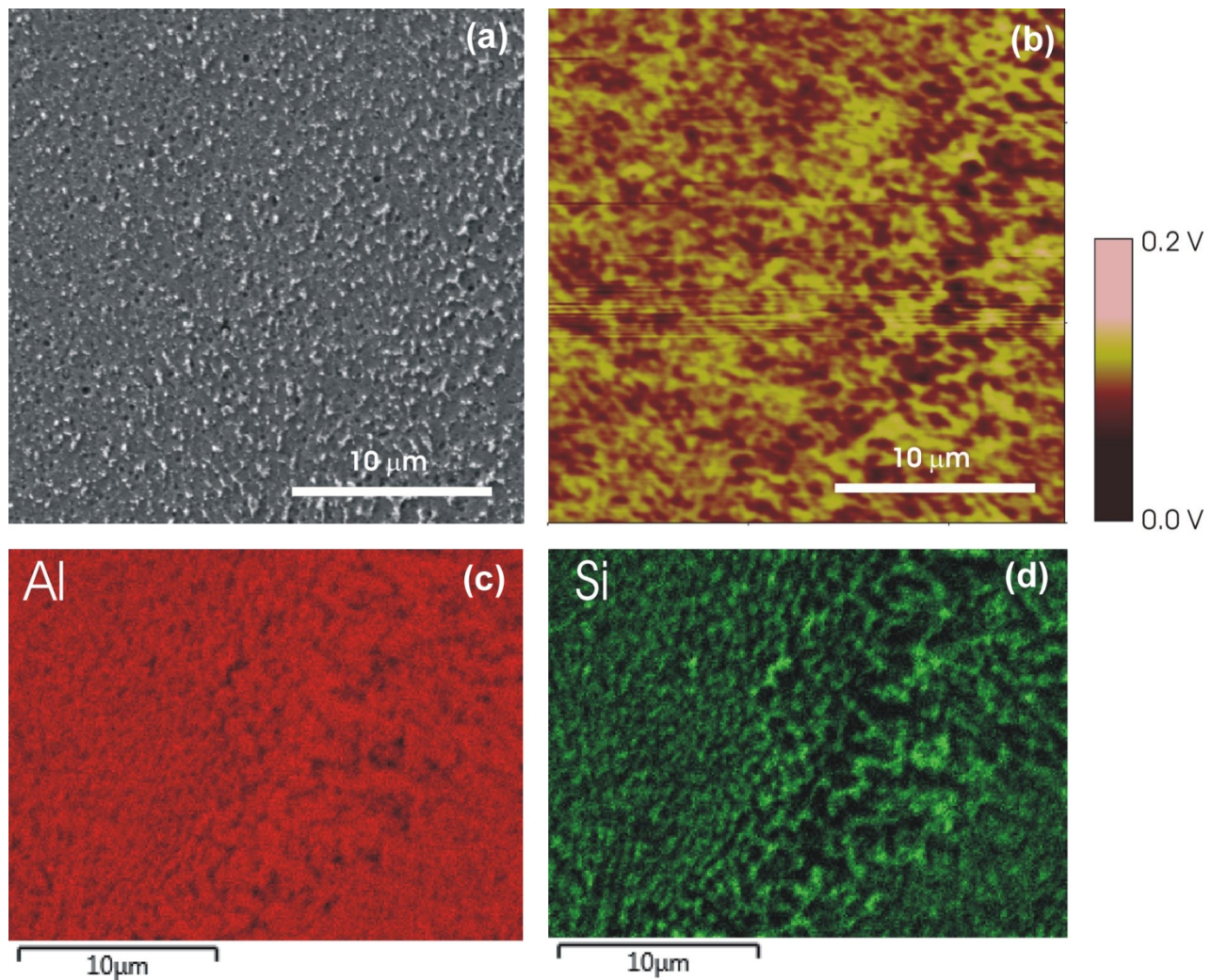


Fig. 9. (a) SEM image, (b) SKPFM potential map, and EDS maps of (c) Al and (d) Si for a polished AlSi10Mg LPBF sample.

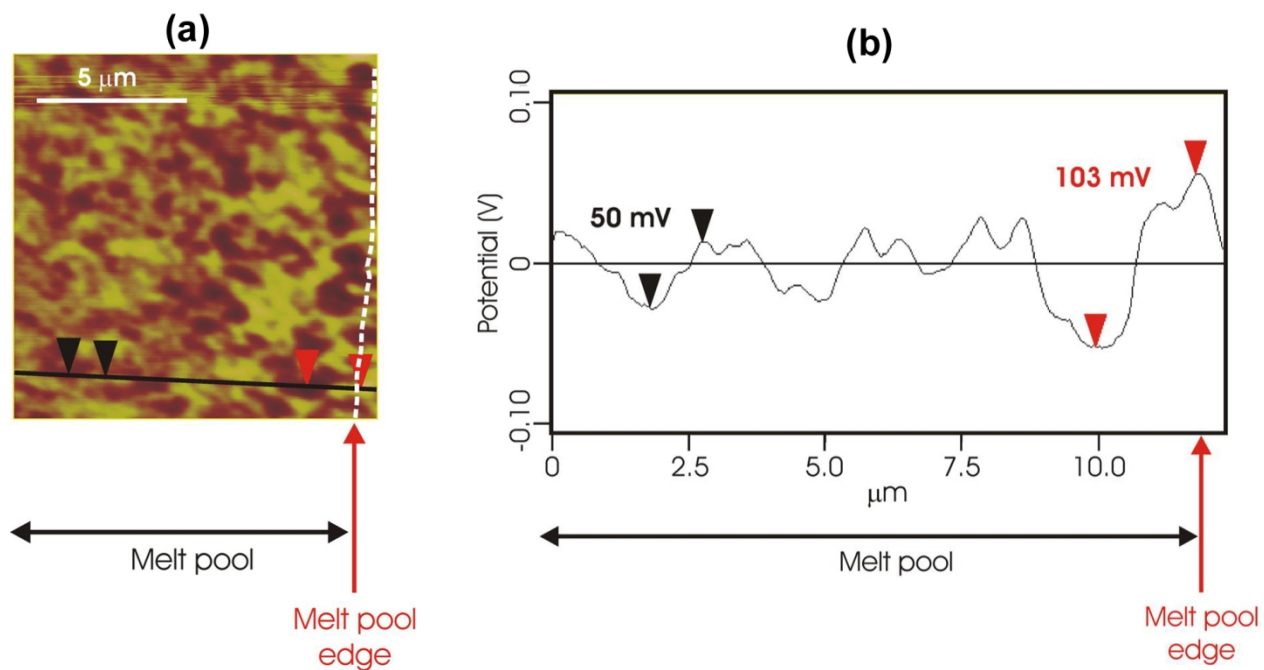
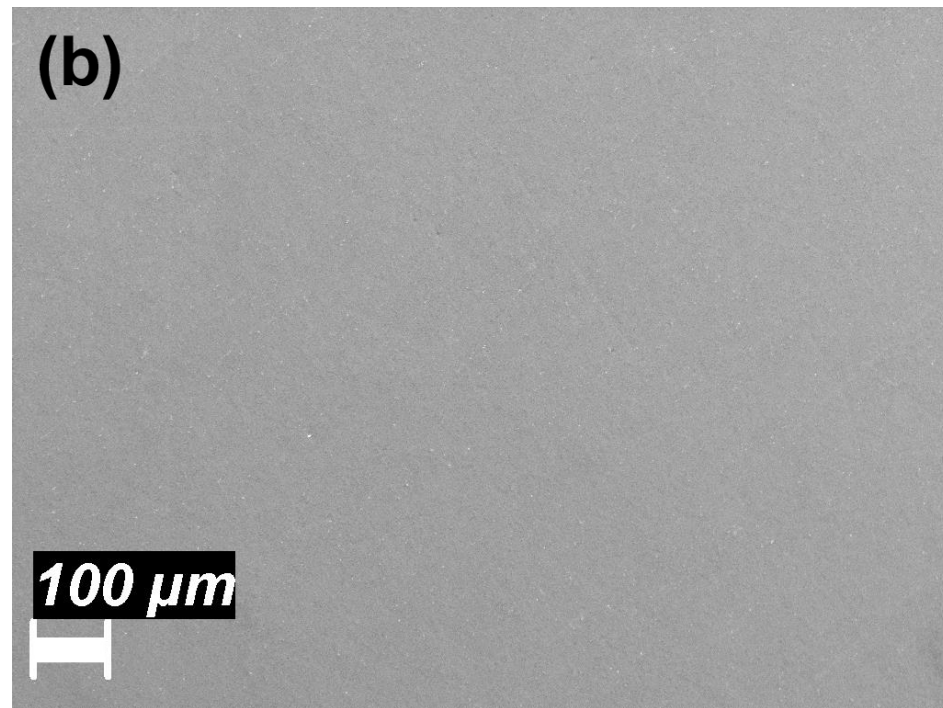
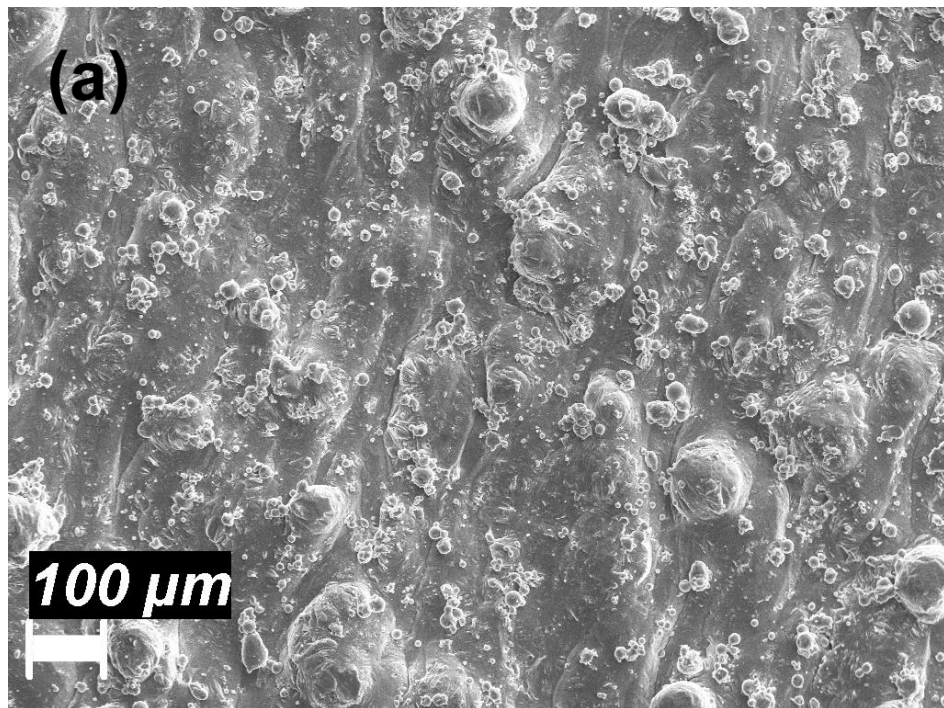
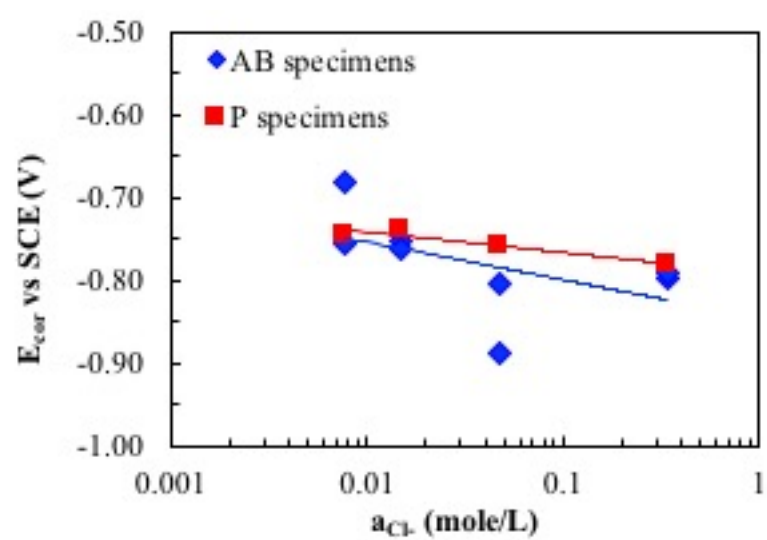
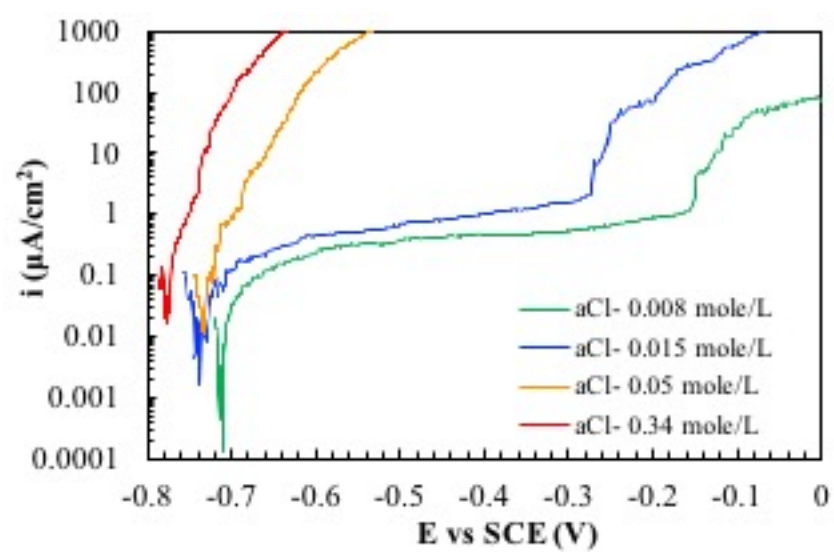
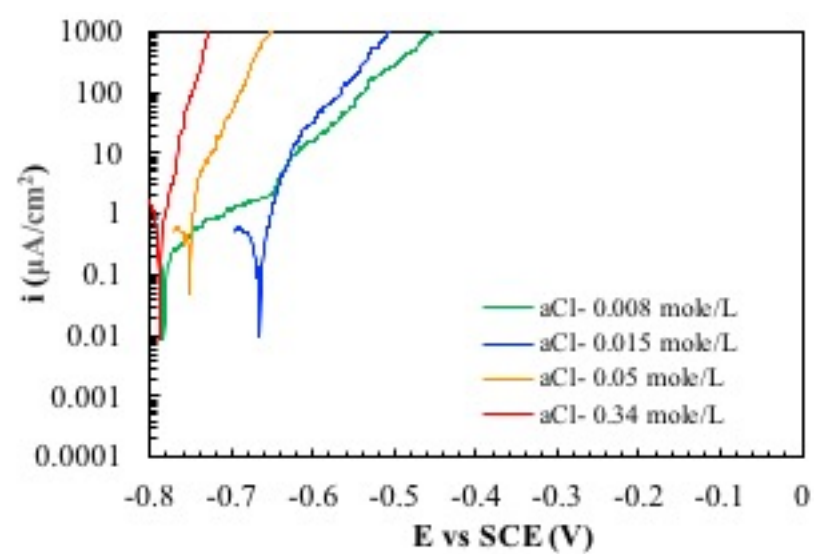


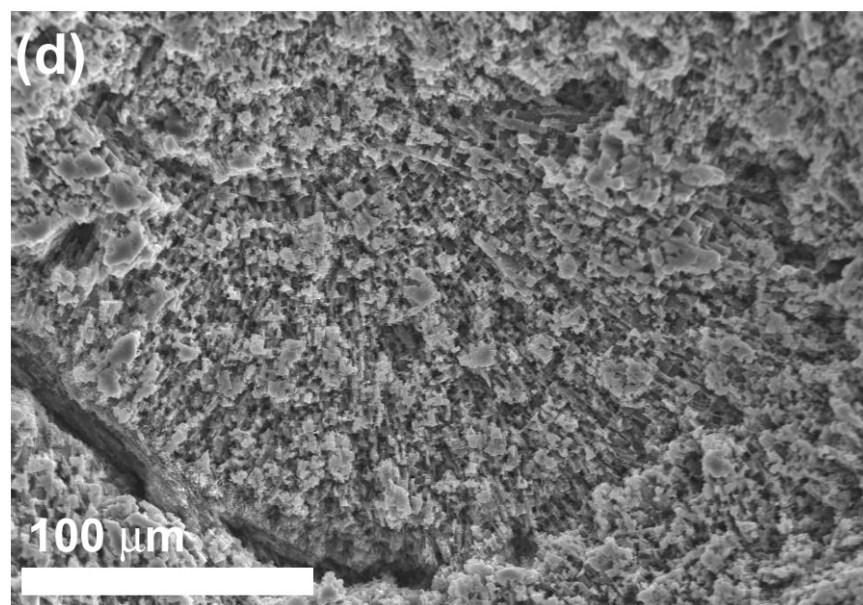
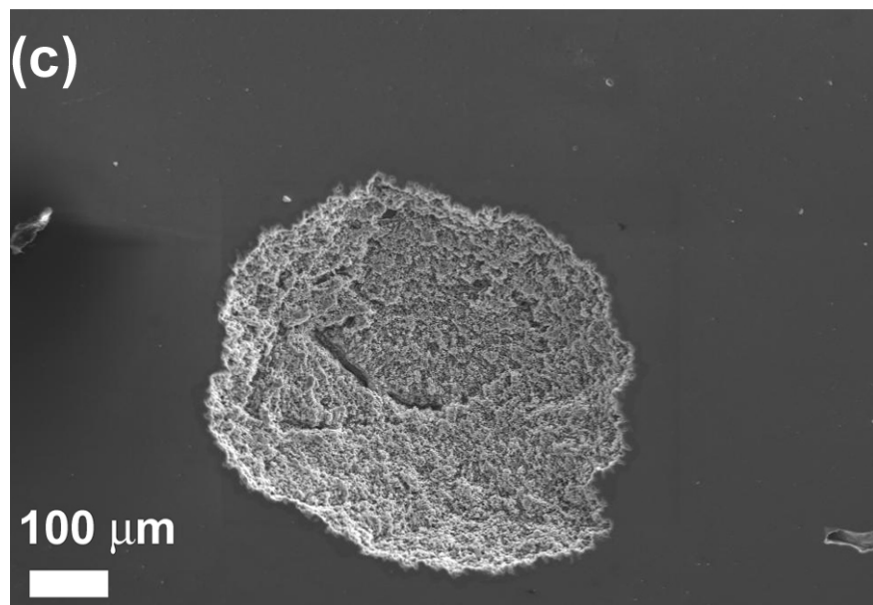
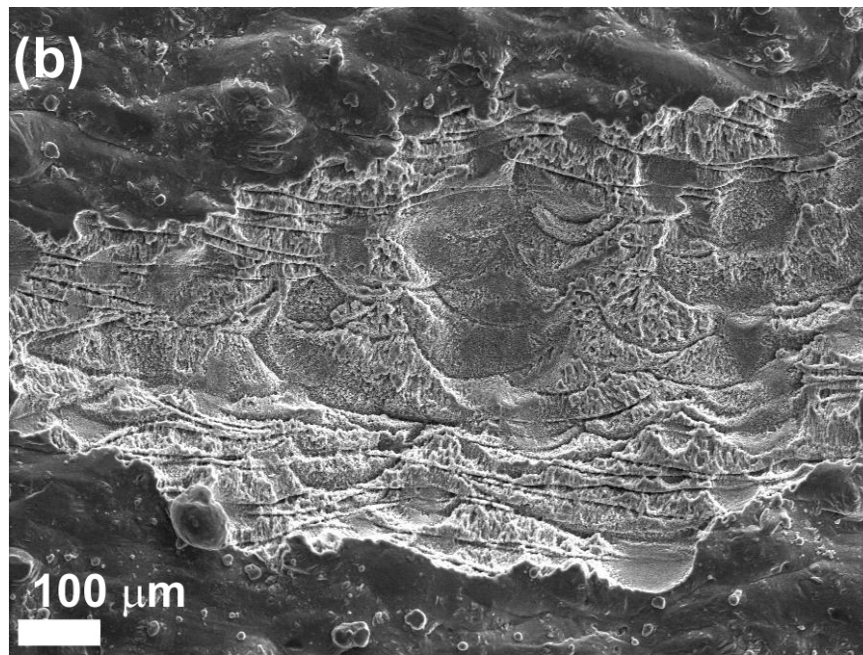
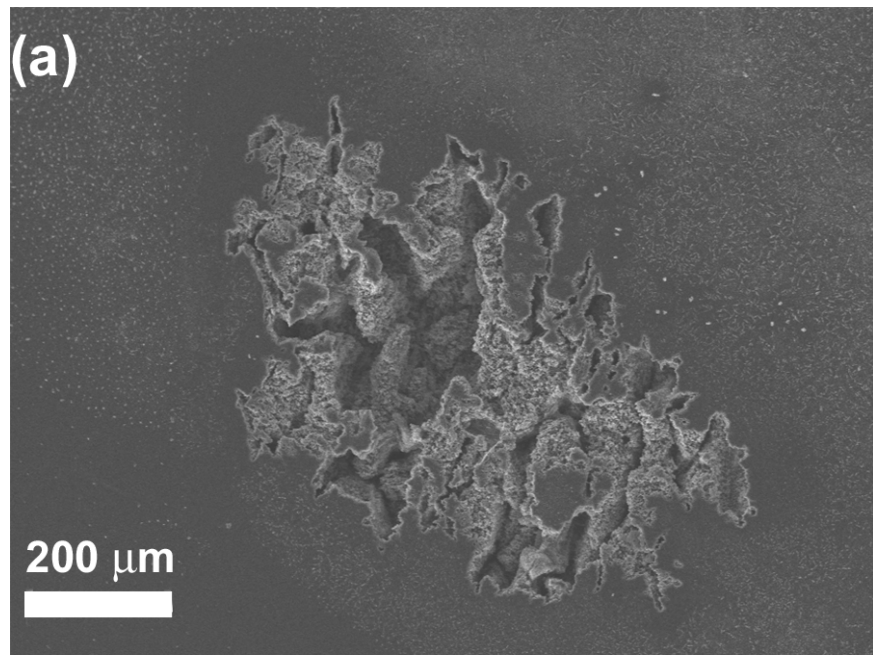
Fig. 10. (a) SKPFM potential map of a region near the edge of a melt pool (indicated by the white dashed line) and (b) the corresponding potential profile along the black line indicated in (a).

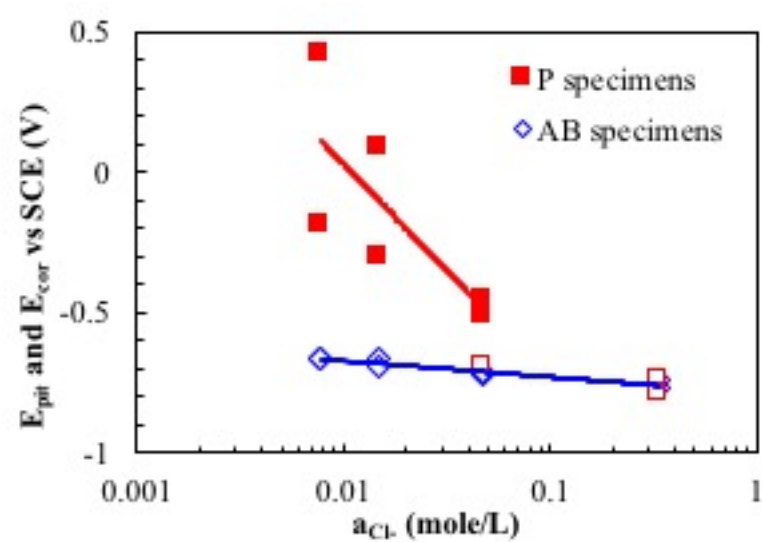


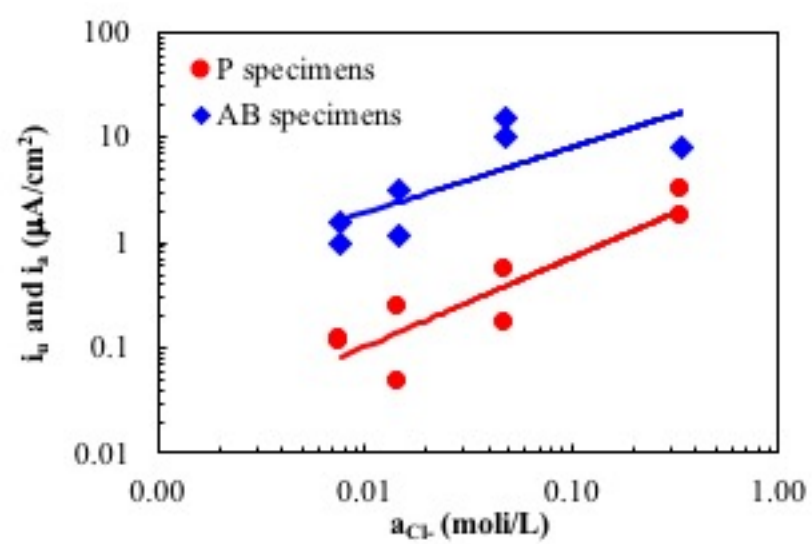


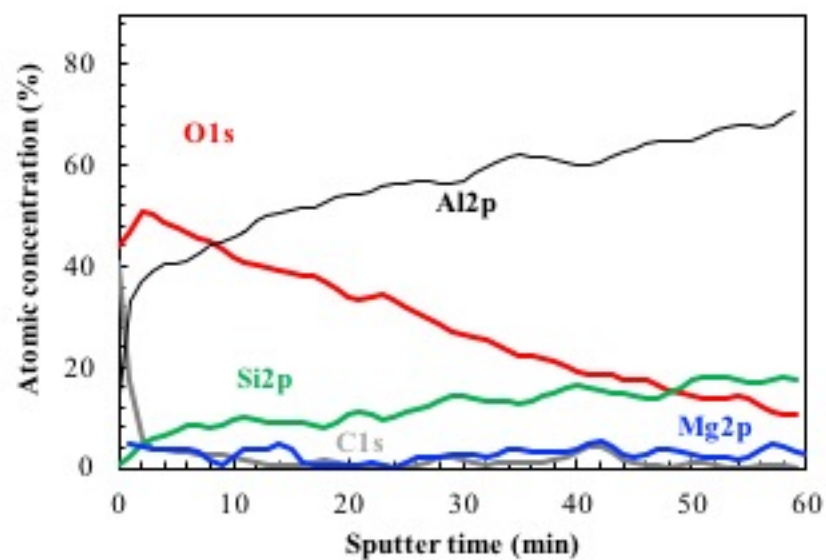


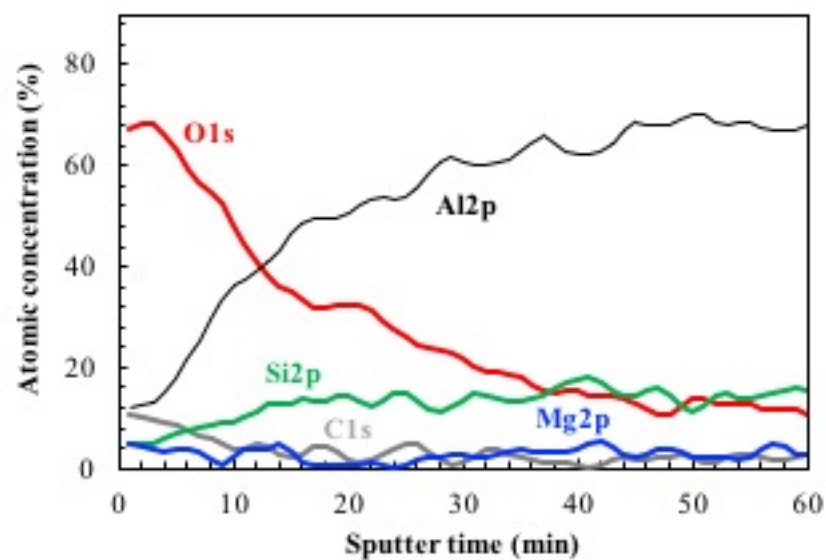


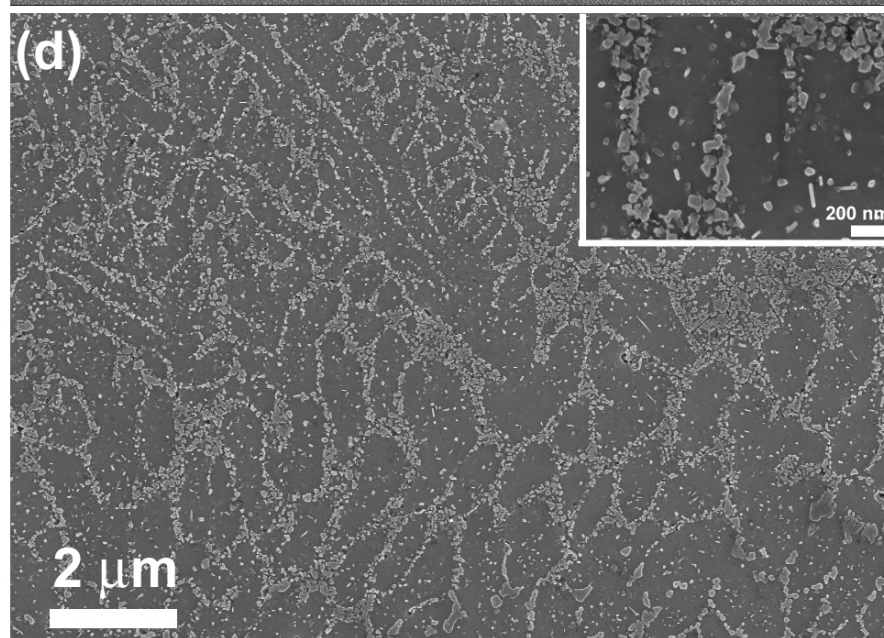
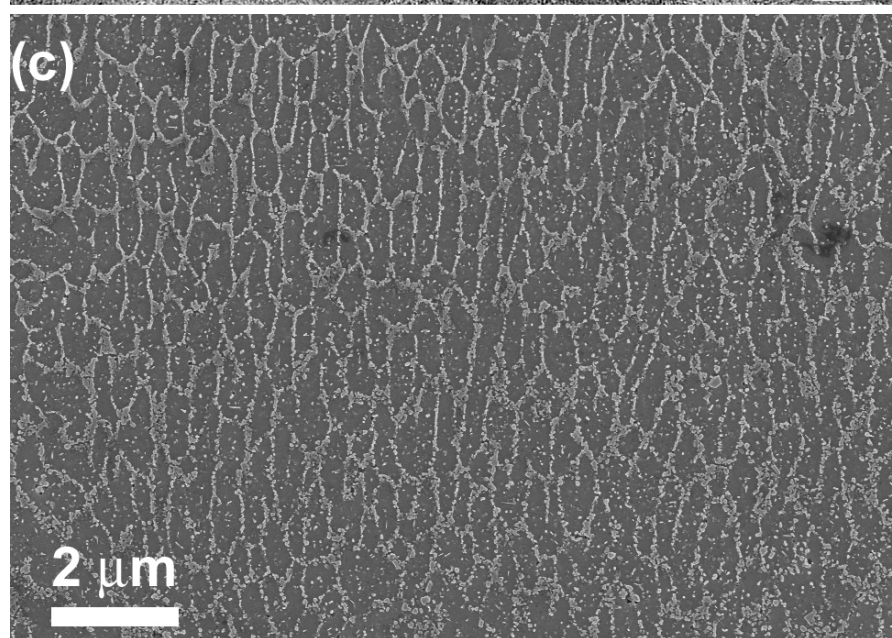
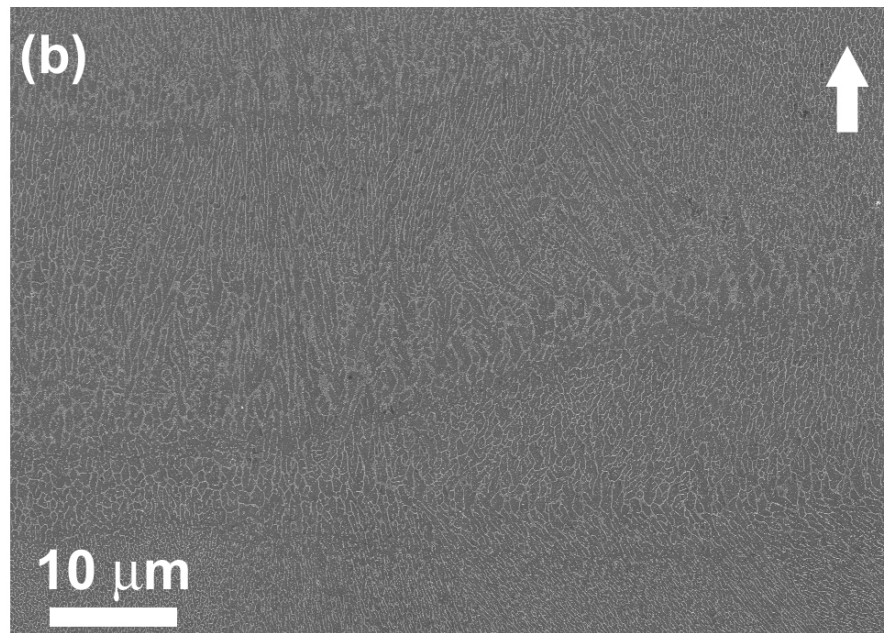
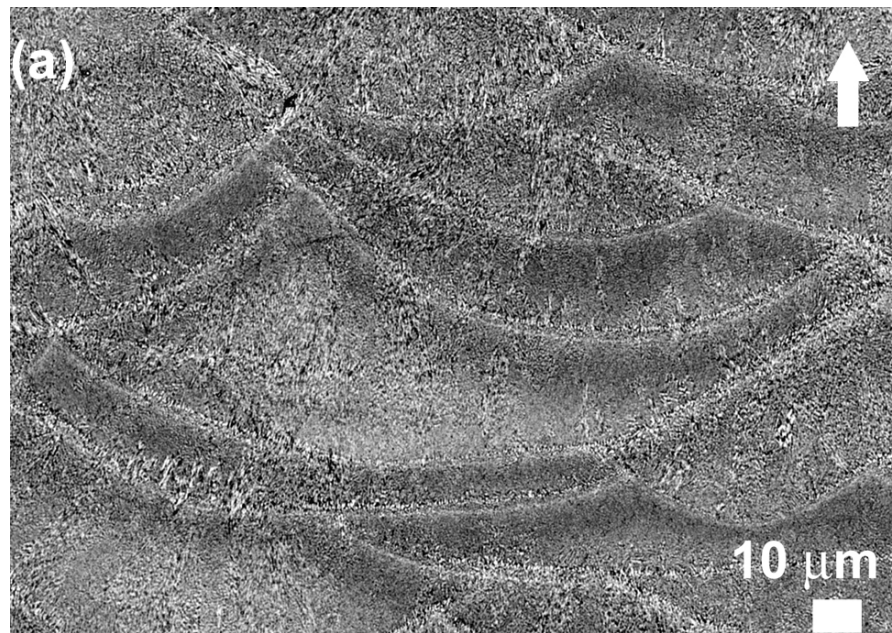


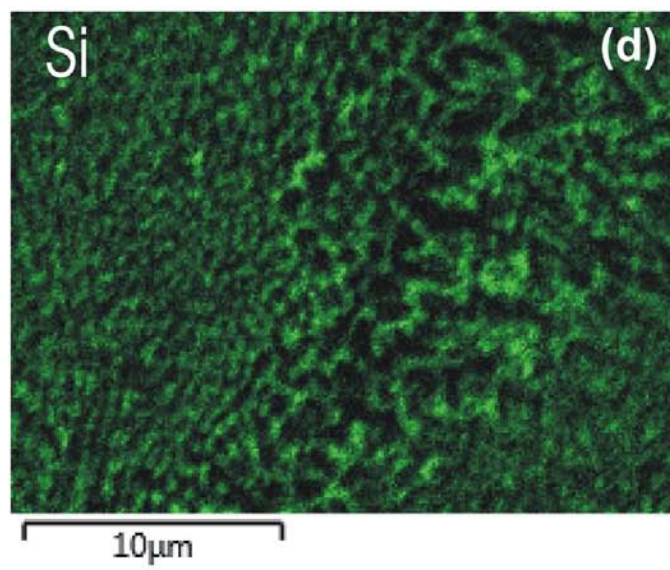
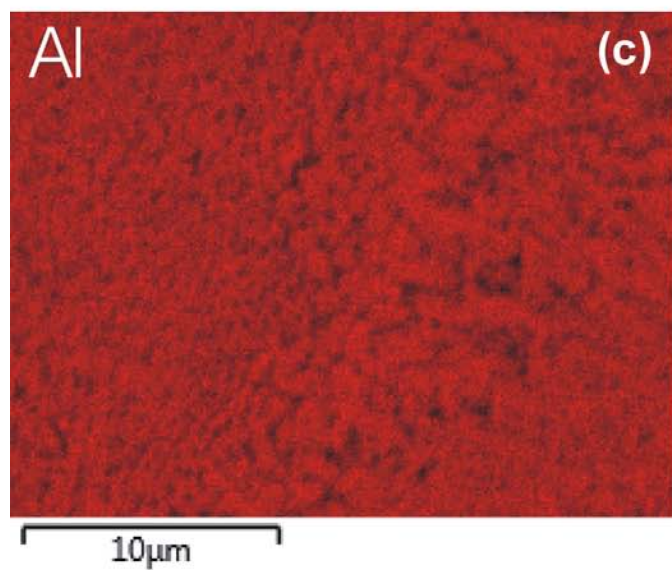
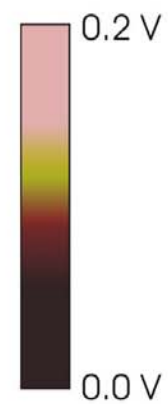
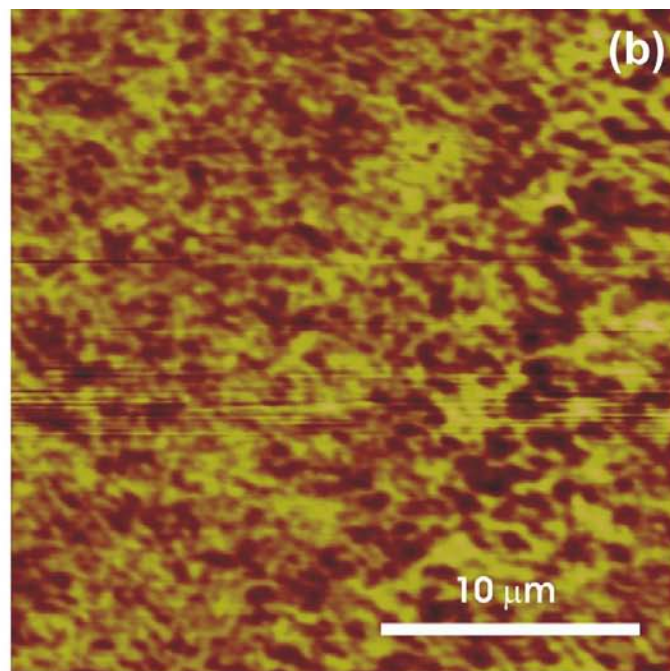
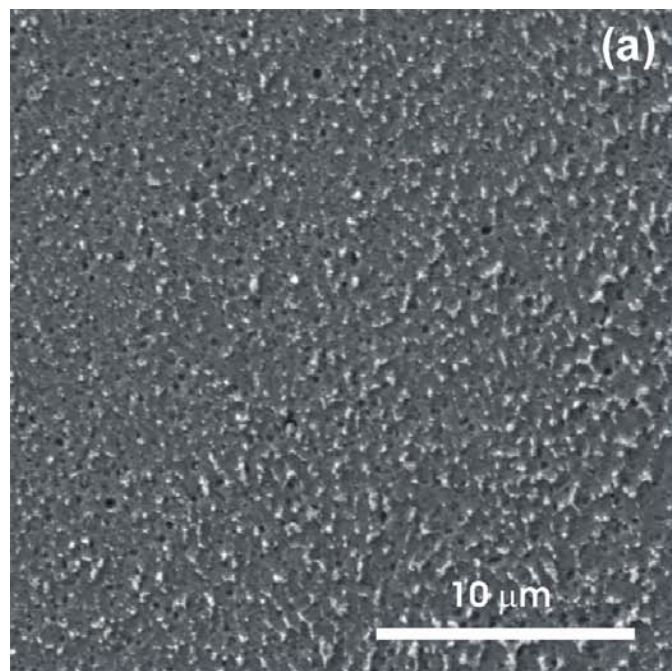




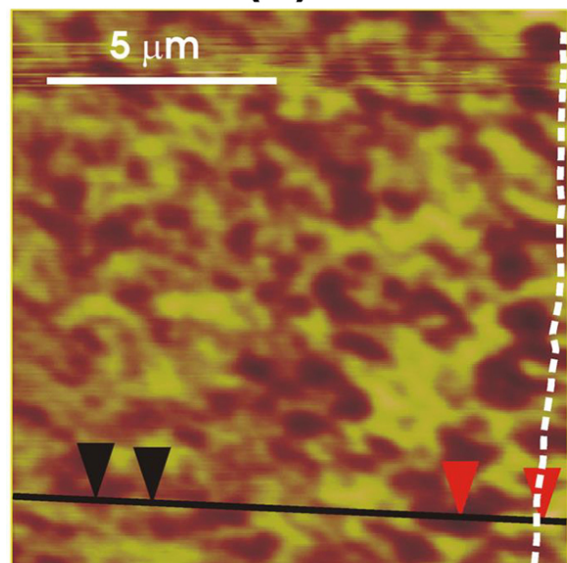








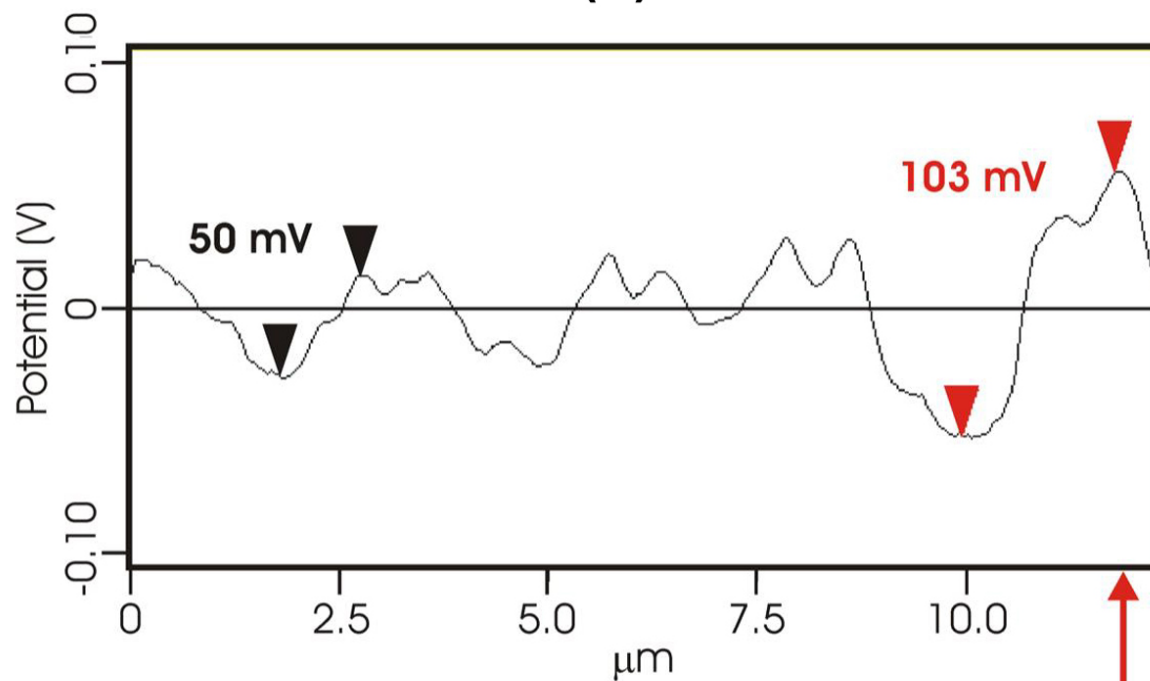
(a)



Melt pool

Melt pool
edge

(b)



Melt pool

Melt pool
edge